



PAPER

Acoustic radiation force induced resonance elastography of coagulating blood: theoretical viscoelasticity modeling and *ex vivo* experimentation

RECEIVED
11 December 2017REVISED
19 February 2018ACCEPTED FOR PUBLICATION
6 March 2018PUBLISHED
21 March 2018Manish Bhatt¹, Emmanuel Montagnon¹, François Destrempes¹, Boris Chayer¹, Siavash Kazemirad² and Guy Cloutier^{1,3,4} ¹ Laboratory of Biorheology and Medical Ultrasonics, University of Montreal Hospital Research Center (CRCHUM), Montréal, Québec H2X 0A9, Canada² School of Mechanical Engineering, Iran University of Science and Technology, Narmak, Tehran 16846-13114, Iran³ Institute of Biomedical Engineering, University of Montreal, Montréal, Québec H3C 3J7, Canada⁴ Department of Radiology, Radio-Oncology and Nuclear Medicine, University of Montreal, Montréal, Québec H3T 1J4, CanadaE-mail: guy.cloutier@umontreal.ca**Keywords:** ultrasonography, dynamic elastography, acoustic radiation force, shear waves, blood rheology, deep vein thrombosis

Abstract

Deep vein thrombosis is a common vascular disease that can lead to pulmonary embolism and death. The early diagnosis and clot age staging are important parameters for reliable therapy planning. This article presents an acoustic radiation force induced resonance elastography method for the viscoelastic characterization of clotting blood. The physical concept of this method relies on the mechanical resonance of the blood clot occurring at specific frequencies. Resonances are induced by focusing ultrasound beams inside the sample under investigation. Coupled to an analytical model of wave scattering, the ability of the proposed method to characterize the viscoelasticity of a mimicked venous thrombosis in the acute phase is demonstrated. Experiments with a gelatin-agar inclusion sample of known viscoelasticity are performed for validation and establishment of the proof of concept. In addition, an inversion method is applied *in vitro* for the kinetic monitoring of the blood coagulation process of six human blood samples obtained from two volunteers. The computed elasticity and viscosity values of blood samples at the end of the 90 min kinetics were estimated at 411 ± 71 Pa and 0.25 ± 0.03 Pa · s for volunteer #1, and 387 ± 35 Pa and 0.23 ± 0.02 Pa · s for volunteer #2, respectively. The proposed method allowed reproducible time-varying thrombus viscoelastic measurements from samples having physiological dimensions.

1. Introduction

Deep venous thrombosis (DVT) is the formation of a blood clot in the deep veins of the lower limbs (Hirsh and Hoak 1996, Weisel 2008, Esmon 2009). This disease is common with an extent of 1 in 1000 person-years (Naess *et al* 2007). The clot release in the venous system can trigger pulmonary embolism, which is the main complication of DVT (White 2003). Associated risk factors for DVT are surgery, trauma, hospital or nursing home confinement, cancer with or without chemotherapy (Heit *et al* 2000), and coagulation disorders (Heijboer *et al* 1990, Goldenberg and Manco-Johnson 2008). The heparin or thrombectomy treatment of DVT succeeds only during the first 7–10 d following the event (Siebers *et al* 2004, Galanaud *et al* 2013), thus accurate age determination of DVT is important. However, popular diagnostic methods such as sonography, phlebography, computed tomography and magnetic resonance tomography often do not provide enough staging accuracy (Mumme *et al* 2002). The clinical gold standard for DVT diagnosis is x-ray venography but it requires injecting potentially allergenic radiopaque contrast agents (Karande *et al* 2016). According to current practice, the development of alternative techniques is desired for more accurate staging of DVT.

Ultrasound-based elastography methods have been proposed to assess mechanical properties of the thrombus, using either static compression (Emelianov *et al* 2002, Xie *et al* 2004, 2005, Rubin *et al* 2006) or shear-wave viscoelasticity technologies (Genisson *et al* 2006a, Schmitt *et al* 2011, Bernal *et al* 2012, 2013, Huang *et al* 2013,

Mfoumou *et al* 2014). Various techniques relying on the measurement of induced displacements at the focal zone of an acoustic beam have also been proposed. One such example is the sonorheometry technique, which assesses the relative elasticity and viscosity of clotting blood (Viola *et al* 2004). Remote vibration of a sphere embedded in the investigated medium was also used to model the relaxation process to estimate viscoelastic properties of hydrogels (Orescanin *et al* 2009). Huang *et al* (2011) extended the application field of a previously established theoretical model describing the motion of a solid sphere (Aglyamov *et al* 2007) to measure viscoelastic properties of blood clots. There have also been recent developments with optical elastography techniques to measure whole blood coagulation (Hajjarian *et al* 2015, Xu *et al* 2016). Interested readers can refer to Benes *et al* (2015) and Anand and Rajagopal (2017) for comprehensive reviews on advances in blood rheology.

Mechanical resonance of a cylindrical soft heterogeneity induced by shear-horizontal waves was also proposed to quantitatively assess blood clot viscoelasticity (Schmitt *et al* 2013). An advantage of the latter approach was the strong dependency of the resonance spectrum on blood clot diameter. However, the proposed approach only allowed quantifying blood clot elasticity as the viscosity had to be assumed when solving the inverse problem based on finite-element method simulations. Aiming *in vivo* viscoelastic characterization of blood clots, the abovementioned quantitative methods are limited either by the required large sample volume to allow proper tracking of shear waves, or by the need of introducing an embedded sphere with known mechanical properties in the blood sample. This paper presents a new viscoelastic characterization method called acoustic radiation force induced resonance elastography (ARFIRE) derived from shear wave induced resonance elastography (SWIRE) concepts (Hadj Henni *et al* 2010, 2012, Schmitt *et al* 2013), with an aim to study blood clots in the acute phase of DVT. ARFIRE distinguishes itself from SWIRE in a way that the acoustic radiation force excitation is performed inside the targeted tissue to generate shear waves, while SWIRE (Hadj Henni *et al* 2010, Schmitt *et al* 2013) generated shear horizontal waves with respect to the long axis of the inclusion by the vibration of a rigid plate or by a needle to simulate a radiation pressure on a line segment. Further, with ARFIRE, shear vertical (SV-) waves are generated perpendicular to the long axis of the inclusion instead of torsional waves as in Hadj Henni *et al* (2012). The analytical ARFIRE model used for the inverse problem solution of SV-wave scattering had to consider two orthogonal coordinate systems. Its solution could be resolved by introducing the Graf's addition theorem for Hankel functions and a Kirchhoff's approximation for wave scattering modeling.

The remaining of this article is organized as follows. Section 2.1 describes a theoretical model for the computation of resonance frequencies of small-diameter cylindrical clots, also referred as inclusions. The inverse problem to compute the viscoelastic properties from spectral resonances is also discussed. In section 2.2, experiments on a gelatin-agar phantom and the application of the proposed method to monitor human whole blood coagulation of blood samples from two healthy volunteers are presented. Section 2.3 describes the signal processing steps and the approach to formulate the inverse problem. Results pertaining to viscoelasticity measurement are presented in section 3, and 4 investigates the robustness of the proposed method and discusses the observations on reproducibility of experimental results and the effect of various parameters, which could affect the accuracy of the viscoelastic characterization. Finally, the conclusion of the study is given in section 5.

2. Methods and materials

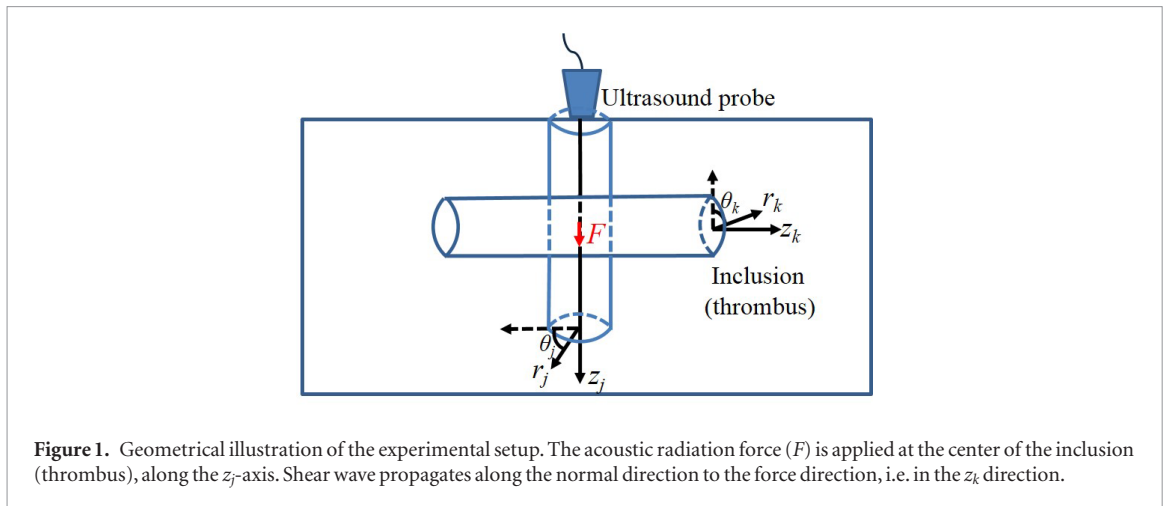
2.1. Theoretical modeling

The acoustic radiation force, which is concentrated along the focused ultrasound beam axis for a few millimeters length, produces an approximate cylindrical shear wave in the medium (Andreev *et al* 1997). Navier's equation governing cylindrical wave motion can be used to model the wave propagation, as previously done by Kazemirad *et al* (2016). The direction of particles' displacement is perpendicular to the shear-wave propagation direction. The cylindrical shear waves produced by an acoustic radiation force concentrated along the z -axis of the cylindrical coordinates can be given as Graff (1991) and Kazemirad *et al* (2016)

$$U_{\text{inc}}(r_j, \omega) = A_1(\omega) \frac{i}{4} H_0^1(k_s r_j), \quad (1)$$

where U_{inc} is the displacement vector in z_j direction, and r_j is the propagation distance in the radial direction of the assumed cylindrical coordinate system, as represented in figure 1. Parameter ω denotes the angular frequency, $A_1(\omega)$ is related to the amplitude of shear waves at different frequencies, $H_0^1(\cdot)$ is the Hankel function of the first kind of order zero, and $k_s = \sqrt{\frac{\rho\omega^2}{G}}$ is the shear wavenumber, where ρ is the density of the medium and G is the second Lamé coefficient. Recall that, in linear viscoelasticity, G also refers to the complex shear modulus $G = G' + iG''$, where G' and G'' are storage and loss moduli, respectively.

As illustrated in figure 1, the ultrasound probe that is used to generate the acoustic radiation force is placed perpendicular to the z_k -axis of the cylindrical inclusion (thrombus). Equation (1) is expressed with respect to the z_j -axis of the acoustic push. This results in two cylindrical coordinate systems, one parallel (see (r_k, θ_k, z_k)) and another perpendicular (see (r_j, θ_j, z_j)) to the inclusion. To carry on theoretical computations, only one coordinate



system should be used, and so, equation (1) will be transformed to the cylindrical coordinate system of the inclusion. In order to carry on the corresponding transformations of Hankel functions, we propose an original use of Graf's addition theorem (Erdeyli 1968, Abramowitz and Stegun 1980) in this framework. The Graf's addition theorem for cylindrical Bessel functions, which states that a displaced cylindrical harmonic function is a linear superposition of undisplaced cylindrical harmonic functions, can be written as (for $|ve^{i\alpha}| < |u|$)

$$H_n(w) e^{in\chi} = \sum_{m=-\infty}^{\infty} H_{n+m}(u) J_m(v) e^{im\alpha}, \quad (2)$$

where α is the angle between sides u and v , and χ is the angle between sides u and w of a triangular system, as discussed in appendix A. Using this theorem, the cylindrical shear wave of equation (1) can be expressed in the (r_k, θ_k, z_k) coordinate system as (details in appendix A),

$$U_{\text{inc}}(r_k, \omega) = A_1(\omega) \frac{i}{4} \sum_{m=-\infty}^{\infty} J_m(k_s z_k) H_m^{(1)}(k_s r_k \sin\theta_k) e^{\frac{im\pi}{2}}. \quad (3)$$

The incident wave, which is expressed by equation (3), is produced inside the inclusion (thrombus) by the acoustic radiation force. When this wave reaches the boundary of the inclusion, a part of it is reflected, and the remaining part is transmitted to outside the inclusion. At this frontier, two boundary conditions (continuity of displacement and stress) can be utilized to compute the characteristic wave coefficients of the inclusion and surrounding medium (Hadj Henni *et al* 2012).

A straightforward way to write reflected and transmitted wave equations at any boundary point is by using tangential plane approximation, also known as Kirchoff's approach (Yamada and Hidaka 2005). This approach approximates a curved boundary at any point by a tangent plane (Voronovich 1999), and thus, the field computation is done as if the surface were to be replaced by its tangent plane at that point. Now, similar to Aki and Richards (1980), the reflected wave from a tangential plane that is normal to the direction of the $r_k \sin\theta_k$ vector can be expressed as

$$U_{\text{ref}}(r, \omega) = A_2(\omega) \sum_{m=-\infty}^{\infty} J_m(k_s z_k) H_m^{(1)}(k_s r_k \sin\theta_k e^{i\pi}) e^{\frac{im\pi}{2}}, \quad (4)$$

and the transmitted wave,

$$U_{\text{trans}}(r, \omega) = B_1(\omega) \sum_{m=-\infty}^{\infty} J_m(k_s z_k) H_m^{(1)}(k'_s r_k \sin\theta_k) e^{\frac{im\pi}{2}}. \quad (5)$$

Here, k'_s corresponds to the shear wavenumber of the surrounding medium. $A_2(\omega)$ and $B_1(\omega)$ are reflection and transmission coefficients, respectively. The first boundary condition, i.e. the continuity of displacement, which is written as

$$U_{\text{inc}} + U_{\text{ref}} = U_{\text{trans}} \quad (6)$$

can now be applied at any suitable point such as $z_k = 0; \theta_k = \pi/2$, in the plane $r_k = r_0$, where r_0 is the radius of the inclusion. Substituting equations (3)–(5) in (6) simplifies to

$$\frac{i}{4} H_0^{(1)}(k_s r_0) - \frac{A_2(\omega)}{A_1(\omega)} H_0^{(2)}(k_s r_0) = \frac{B_1(\omega)}{A_1(\omega)} H_0^{(1)}(k'_s r_0). \quad (7)$$

Note that the following two identities have been used in the above step (Abramowitz and Stegun 1980, Jentschura and Lotstedt 2011):

$$J_m(0) = \begin{cases} 1, & m = 0 \\ 0, & m \in \mathbb{Z}, m \neq 0 \end{cases}; \quad (8)$$

$$H_n^{(1)}(xe^{i\pi}) = -e^{-in\pi} H_n^{(2)}(x). \quad (9)$$

Equation (7) can be rewritten as

$$H_0^{(1)}(k_s r_0) - A(\omega) H_0^{(2)}(k_s r_0) = B(\omega) H_0^{(1)}(k'_s r_0), \quad (10)$$

where the normalized parameters $A(\omega) = \frac{4}{i} \frac{A_2(\omega)}{A_1(\omega)}$, and $B(\omega) = \frac{4}{i} \frac{B_1(\omega)}{A_1(\omega)}$ are related to reflection and transmission coefficients of the wave propagation within both media. Equation (10) is the first boundary condition with two unknown coefficients, i.e. $A(\omega)$ and $B(\omega)$.

The second boundary condition, the continuity of stress (σ) at the same point in the plane $r_k = r_0$, can be expressed as Morse and Feshbach (1953) and Hadj Henni *et al* (2012)

$$\sigma_{\text{inc}} + \sigma_{\text{ref}} = \sigma_{\text{trans}}. \quad (11)$$

For homogenous linear viscoelastic media, the stress tensor (σ) can be computed using the strain gradient theory. This theory for a cylindrical coordinate system has been described in detail by Zhao and Pedroso (2008). In simple words, if ϵ is the strain tensor and C is the symmetric stiffness tensor, the stress-strain relationship in the matrix form is given as

$$\sigma = C\epsilon,$$

$$\begin{bmatrix} \sigma_{rr} \\ \sigma_{\theta\theta} \\ \sigma_{zz} \\ \sigma_{r\theta} \\ \sigma_{\theta z} \\ \sigma_{rz} \end{bmatrix} = \begin{bmatrix} C_{rr} & C_{r\theta} & C_{r\theta} & & & \\ C_{\theta r} & C_{rr} & C_{r\theta} & & & \\ C_{\theta r} & C_{\theta r} & C_{rr} & & & \\ & & & \frac{C_{rr}-C_{r\theta}}{2} & 0 & 0 \\ & 0 & & 0 & \frac{C_{rr}-C_{r\theta}}{2} & 0 \\ & & & 0 & 0 & \frac{C_{rr}-C_{r\theta}}{2} \end{bmatrix} \begin{bmatrix} \epsilon_{rr} \\ \epsilon_{\theta\theta} \\ \epsilon_{zz} \\ \epsilon_{r\theta} \\ \epsilon_{\theta z} \\ \epsilon_{rz} \end{bmatrix}, \quad (12)$$

where subscripts r, θ, z denote the tensor components in that direction. The details of the computation of right-hand side terms are given in appendix B. A linear equation for the continuity of the stress boundary condition is obtained using equations (11) and (12), which is

$$G_{\text{inc}} \frac{\partial u_{\text{inc}}}{\partial r} + G_{\text{inc}} \frac{\partial u_{\text{ref}}}{\partial r} = G_{\text{surr}} \frac{\partial u_{\text{trans}}}{\partial r}, \quad (13)$$

as explained in appendix B. Here, G_{inc} denotes the second Lamé coefficient of the inclusion and G_{surr} that of the surrounding medium. $A(\omega)$ and $B(\omega)$ appear in this equation when the partial derivatives are evaluated. Thus, using the two boundary conditions of displacement (equation (10)) and stress continuities (equation (13)), a linear system is obtained and solved to determine the parameters $A(\omega)$ and $B(\omega)$, and consequently displacements of incident, reflected and transmitted waves. Since $A(\omega)$ and $B(\omega)$ are normalized parameters, displacements obtained are also normalized, which is sufficient to find the resonant frequency of the inclusion; i.e. the frequency when particle displacement (or normalized displacement) is maximum.

2.1.1. Resonance properties

Shear waves generated inside the inclusion (blood clot) are simultaneously reflected and transmitted to the surrounding medium at its boundary. For discrete frequencies, constructive interferences occur inside the inclusion, leading to a mechanical resonance phenomenon. As demonstrated by Hadj Henni *et al* (2010), resonance frequencies (or eigenfrequencies) depend on mechanical properties of propagating media and inclusion dimensions. With some prior information, identification of eigenfrequencies can allow estimation of the storage shear modulus of the inclusion, as demonstrated by Schmitt *et al* (2013). However, for a viscoelastic inclusion, viscosity acts as a damper and low-pass filter, shifting resonance frequencies toward lower values. Therefore, identifying resonance frequencies alone is not sufficient to simultaneously estimate the elasticity and viscosity of the insonified medium. Henceforth, one more parameter is required for formulating a cost function to compute both elasticity and viscosity components.

To estimate the inclusion's viscosity, the displacement spectrum can be used as an additional parameter. An inversion model involving a cost function which minimizes the distance between experimental and theoretical spectral characteristics is utilized in this study. These spectral characteristics are: (a) the first resonance frequency (f_1); and, (b) its half-width at half maximum (HWHM), labeled as $B_{1/2}$. Using the proposed analytical model, the particle displacement is computed and the resonance frequency can be estimated (which corresponds to the maximum displacement). Thus, theoretical values of f_1 and $B_{1/2}$ are pre-computed and mapped into a lookup table ($f_1^{\text{th}}(r_0, \mu, \eta)$, $B_{1/2}^{\text{th}}(r_0, \mu, \eta)$), where superscript *th* implies theoretical values, r_0 is the cylindrical blood clot radius, μ is the shear elasticity, and η is the viscosity.

Using the theoretical model presented above, resonance frequencies and corresponding HWHM of cylindrical inclusions exhibiting radii ranging from 3 to 8 mm (0.5 mm stepwise), shear elasticity from 50 to 600 Pa (50 Pa stepwise), and viscosities from 0.05 to 0.40 Pa · s (0.05 Pa · s stepwise) were assessed. Such ranges were chosen for blood sample experiments to cover lower limb venous dimensions (Ribreau and Thiriet 1998) and storage shear moduli of fresh acute thrombi (Mfoumou *et al* 2014). Because little data exist on blood clot viscosity, the selected search range was empirical. Blood clot mechanical properties were assessed by the Kelvin–Voigt model in the vicinity of the resonance frequency (i.e. $G = \mu + i\omega\eta$) (Schmitt *et al* 2013). Note that any other rheology models such as Maxwell or Zener can be utilized in place of the Kelvin–Voigt method to describe the viscoelastic behavior of the inclusion. However, the Kelvin–Voigt model was chosen in this study to be in-line with past literature on blood clotting (Gennisson *et al* 2006a, 2006b, Huang *et al* 2013, Schmitt *et al* 2013) and to allow comparing elasticity and viscosity values obtained by them using the same method. The approximate elasticity and viscosity of the surrounding medium mimicking biological tissues around the blood vessel were fixed in the simulations at 5 kPa and 0.15 Pa · s, respectively.

2.2. Experiments

In this study, various experiments were performed with tissue-mimicking phantoms made of gelatin and agar as well as with human blood samples. The gelatin-agar phantom experiments were conducted to validate the mathematical model presented in the previous subsection. However, the main focus of the study was on the kinetic measurement of the viscoelastic properties of clotting blood, for which samples were collected from two healthy female volunteers (27 and 31 years old). This study was approved by the human ethical review committee of the University of Montreal Hospital Research Center and participants signed an informed consent.

2.2.1. Phantom preparation

Two sets of gelatin-agar solutions were prepared: first, to prepare a surrounding medium for both validation and human blood tests and second, to prepare an inclusion sample for the validation test. The tissue mimicking medium surrounding the inclusion was made of one liter of 2% agar (product number A-9799, Sigma Chemical, Saint-Louis, MO, USA) and 3% gelatin (product number G-1890, Sigma Chemical) in water weight concentration. Two distinct 5 mm radius cylindrical holes, 5 cm in height, were embedded into the phantom material to contain 4 ml of inclusion samples (phantom gel and blood samples), as shown in figure 2. Clotting kinetic measurements were made in a controlled environment (20 °C) to prevent potential biases/variations in viscoelasticity due to temperature changes (Valeri *et al* 1995).

The other gelatin-agar viscous phantom to be used as the inclusion sample for the validation test was fabricated with 2.5% gelatin and 3% agar in water weight concentration. To prepare the phantom, gelatin was dissolved in distilled water and the solution was heated up to 90 °C to obtain a homogeneous and clear transparent solution. The solution was allowed to cool down to 50 °C and then agar powder was added. The mixture was then allowed to return naturally to room temperature (20 °C). This mixture was kept overnight in a vacuum chamber and heated at 30 °C on the next morning for about 5 min to bring it to liquid (gel) state, and then it was allowed to gelify while the temperature returned to 20 °C. Details of the experiments are discussed later.

2.2.2. Preparation of blood samples

Each volunteer underwent the following protocol three times over a period of two weeks. Blood was punctured in the morning before food intake. Three ethylene diamine tetraacetic acid (k_2 EDTA) tubes (BD Vacutainer, Becton Dickinson, Franklin lake, NJ, USA) were used for basic hematologic analyses (table 1). The blood samples were sent to the hospital (University of Montreal Hospital Centre) for hematologic tests, where standard clinical coagulation analysis protocol was followed. Additionally, two uncoated red serum tubes (dry tubes) (BD Vacutainer, Becton Dickinson, Franklin lake, NJ, USA) were filled for ARFIRE measurements. The blood was punctured in the experiment room and the tubes were immediately poured into phantom holes within a minute from puncture time, which was defined as the initial time (t_0) for kinetic clotting measurements. ARFIRE measures were launched within 2 min from blood sampling. Because dry tubes were used, the coagulation process occurred naturally and did not require the addition of CaCl_2 or of any other substances to trigger the coagulation

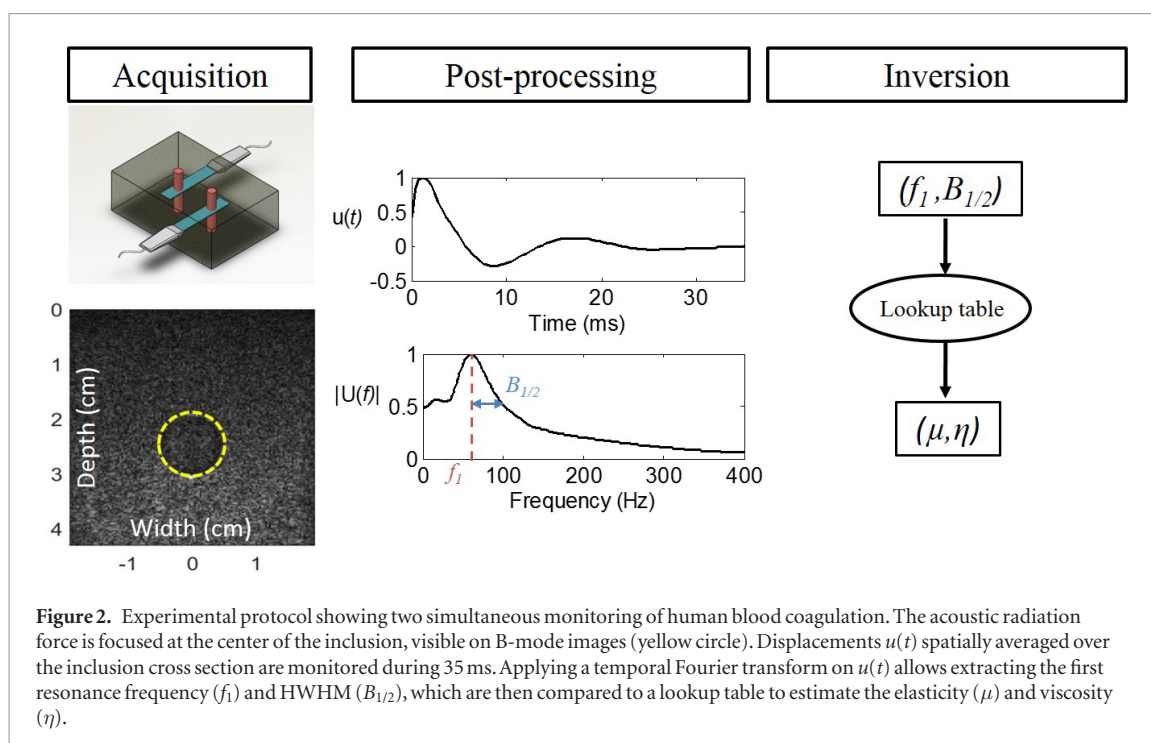


Table 1. Hematologic analyses of both volunteers for each of the three blood samples analyzed.

| Case | Platelets ($10^9/l$) | PT (INR) | CT (s) | TT (s) | Fibrin ($g\ l^{-1}$) | HT (%) |
|----------------------|------------------------|----------------|--------------|--------------|------------------------|--------------|
| A-1 | 256 | 1 | 25 | 16 | 2.64 | 36 |
| A-2 | 252 | 1 | 27 | 16 | 2.75 | 39 |
| A-3 | 252 | 1 | 25 | 16 | 2.83 | 37 |
| B-1 | 238 | 1 | 27 | 18 | 2.42 | 40 |
| B-2 | 240 | 1 | 24 | 16 | 2.40 | 39 |
| B-3 | 240 | 1 | 23 | 17 | 2.25 | 38 |
| <i>Normal ranges</i> | <i>140–450</i> | <i>0.9–1.2</i> | <i>23–29</i> | <i>14–18</i> | <i>2.0–4.5</i> | <i>36–46</i> |

PT: Prothrombine time.

INR: International normalized ratio.

CT: Cephaline time.

TT: Thrombine time.

HT: Hematocrit.

cascade. To evaluate the reproducibility of results, two independent measurements were performed on a given blood sample (withdraw on a given day), resulting in a total of 6 measurements for each volunteer.

2.2.3. Gelatin-agar phantom measurements

Two types of experiments were performed to obtain the preliminary validation of the theoretical model. An illustration of the experimental setups is shown in figure 3. The first experiment (figure 3(a)) was conducted using a commercial rheometer (RheoSpectris C500, Rheolution Inc, Montreal), which directly measures the viscoelasticity of a sample over a period of time (Hadj Henni *et al* 2011). The liquid sample was poured into a cylindrical sample holder, the diameter of which was 9.5 mm. A laser above the sample holder recorded measurements at 100 Hz for a duration of ~ 80 min, granting the sol-gel solution sufficient time to solidify. The rheometer provided 14 viscoelastic measurements during this period.

The second experiment was performed using the plane-wave polarization method, as explained by Catheline *et al* (2004) and Bernard *et al* (2017). This plane-wave method was compared successfully with a gold standard conventional rheometry method for the viscoelastic characterization of soft materials (Genisson *et al* 2014). In brief, a metal plate was embedded into the liquid state gelatin-agar phantom, as illustrated in figure 3(b). The setup was then placed in a temperature-controlled chamber (4°C), where the gel coagulation was followed for 2 h. After coagulation, the setup was naturally allowed to return to the room temperature (20°C). An electronic shaker (type 4810, Brüel and Kjær, Nærum, Denmark) connected to a waveform generator (33250A, Agilent Technologies, Santa Clara, CA, USA) was then used to vibrate the metal plate at 100 Hz to generate shear waves inside the phantom, and ultrasound data were recorded using a Verasonics V-1 scanner (Verasonics Inc.,

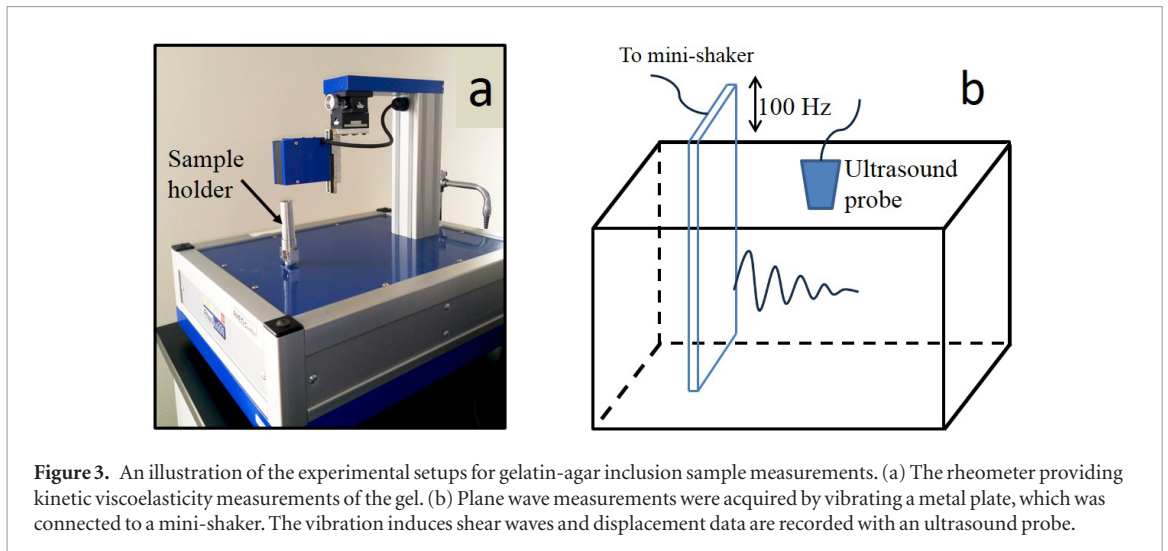


Figure 3. An illustration of the experimental setups for gelatin-agar inclusion sample measurements. (a) The rheometer providing kinetic viscoelasticity measurements of the gel. (b) Plane wave measurements were acquired by vibrating a metal plate, which was connected to a mini-shaker. The vibration induces shear waves and displacement data are recorded with an ultrasound probe.

Redmond, WA, USA). The ultrasound probe tracked planar shear waves at a 2.5 kHz frame rate for 60 ms, immediately after the excitation of the plate. The detailed procedure can be read in Bernard *et al* (2017) or Catheline *et al* (2004). Displacements were tracked and then used to measure the elasticity and viscosity using the Kelvin–Voigt model (Genisson *et al* 2006b).

The third experiment (proposed method) was performed by pouring the gelatin-agar inclusion sample into the 5 mm radius cylindrical holes of figure 2. Ultrasound acquisitions were performed with the Verasonics V-1 scanner. Acoustic bursts (200 μ s, 35 V peak-to-peak amplitude at 5 MHz central frequency) and imaging sequences at a frame rate of 2.5 kHz were transmitted to an ATL L7-4 probe (Philips Healthcare, Andover, MA, USA). For each acquisition, the probe was placed so as to scan the middle of the inclusion cylinder (25 mm from the top and bottom surfaces, see figure 2), at a distance of 25 mm from the face of the transducer. The sample cross section center was aligned with the probe mid width (center of the B-mode image), while the acoustic radiation force focus was generated at the center of the circular inclusion. Before and after the radiation force excitation, radio-frequency (RF) frames were acquired. The ultrasound probe imaged the medium with plane-wave imaging for a duration of 20 ms. The inter-frame axial displacement field was then estimated with a conventional 1D normalized cross-correlation algorithm (Luo and Konofagou 2010). The data acquisition was performed kinetically every 2 min for a duration of 90 min. First resonance frequency and HWHM were computed from the post-processing of the displacement data, see figure 2.

2.2.4. Human blood sample measurements

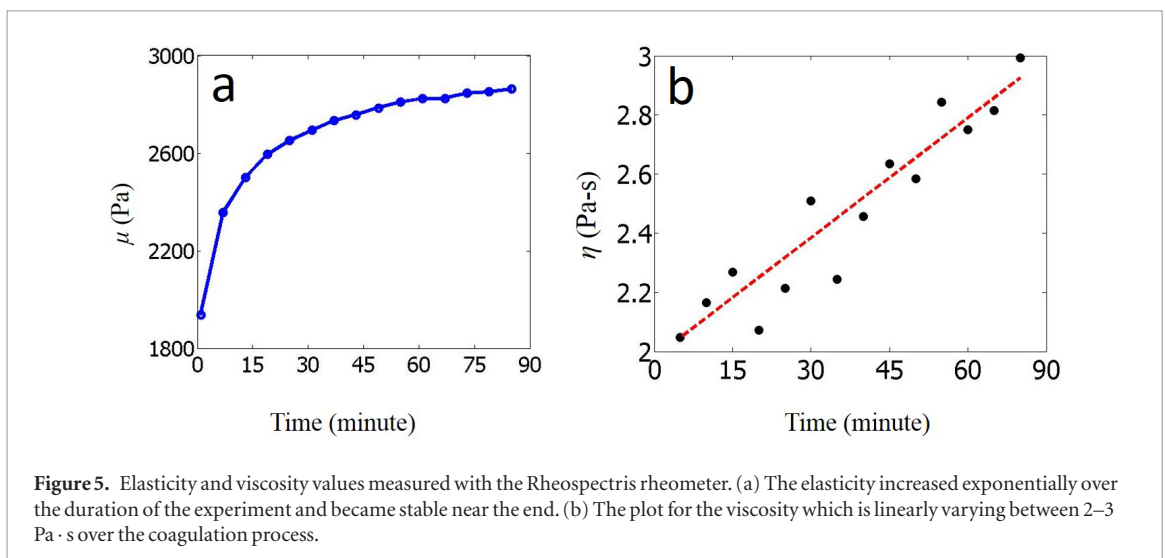
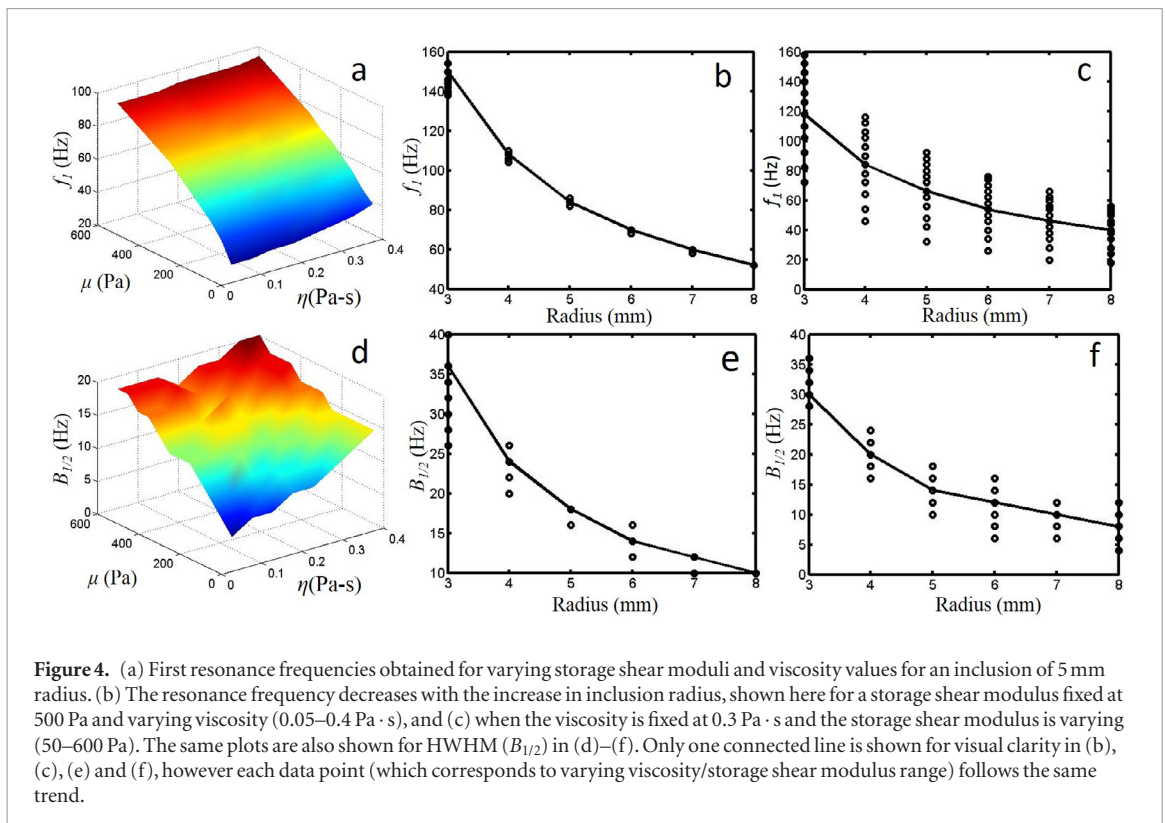
Experiments with human blood samples were also performed using the Verasonics V-1 scanner in a way similar to that mentioned above and presented in figure 2. The ultrasound scanner allowed parallel acquisitions on two distinct samples of a given donor using two L7-4 probes. The coagulation of blood samples was monitored by repeating measurements every 2 min for a duration of 90 min. Acquisitions with probes #1 and #2 were temporally interleaved by a 1 min delay.

2.3. Signal processing

With acquired RF data, radiation force induced displacements were computed using the normalized cross-correlation algorithm (Viola and Walker 2003) implemented on a graphic processing unit (GPU), as described by Montagnon *et al* (2012). For each frame, the spatial mean displacement amplitude over the whole cylinder inclusion cross-section was computed, allowing monitoring the time-varying clotting process (see figure 2). The spatial mean displacement is referred as $u(t)$ in the remaining of this article. To remove any zero-frequency component on $u(t)$, a high-pass first order Butterworth filter with a cut-off frequency of 15 Hz was applied. The first resonance frequency was then assessed by computing the Fourier transform $U(f)$ of $u(t)$. From this spectrum, HWHM (towards the higher frequency range) of the first resonance was also determined, as depicted in figure 2. The choice of HWHM instead of the full width at half maximum relied on observed properties of $U(f)$, as detailed in the discussion section. The previously established lookup table was then used to estimate the elasticity ($G' = \mu$) and viscosity (η) of blood clots by minimizing the following cost function:

$$(\mu_{est}, \eta_{est}) = \operatorname{argmin} \left[\left(f_1^{\text{exp}} - f_1^{\text{th}}(r_0, \mu, \eta) \right)^2 + \left(B_{1/2}^{\text{exp}} - B_{1/2}^{\text{th}}(r_0, \mu, \eta) \right)^2 \right], \quad (14)$$

where subscript *est* means estimated, and superscripts *exp* and *th* refer to experimental and theoretical parameters.



3. Results

3.1. Numerical modelling

As discussed in section 2.3, a look-up table was created to establish the relationship among first resonance frequency and HWHM, and inclusion radius, storage shear modulus (elasticity) and inclusion viscosity. The parameters of the look-up table are plotted in figure 4.

Figure 4(a) depicts the behaviour of the first resonance frequency as a function of the storage shear modulus (elasticity) and viscosity for a fixed inclusion radius of 5 mm. As previously observed (Hadj Henni *et al* 2010), the resonance frequency increases with the storage shear modulus. Figure 4(b) shows the first resonance frequency dependency on the inclusion radius for an elasticity fixed (500 Pa) and varying viscosity (0.05–0.3 Pa · s). The line fitting drawn in the plot is to illustrate this dependency. Data points correspond to multiple viscosity (η) values. It can be observed that there is a slight deviation among different data points, implying that changes in viscosity effect slightly the first resonance frequency. Figure 4(c) depicts the first resonance frequency dependency on the inclusion radius, while the viscosity is fixed (0.3 Pa · s) and the elasticity is varying (50–500 Pa). Unlike figure 4(b), this plot shows significant deviations for given radii, implying a dependence of the first resonance frequency on

Table 2. Elasticity (μ) and viscosity (η) values for a 2.5% gelatin—3% agar phantom obtained from three different experiments (rheometry, plane wave and proposed ARFIRE model). Values are comparable and in the same range, which confirms the validation of the proposed model.

| Parameters | Rheometer data (kinetics) | Plane wave experiment (at plateau) | Proposed model (kinetics) | Genisson <i>et al</i> (2006b) |
|-----------------|---------------------------|------------------------------------|---------------------------|-------------------------------|
| μ (kPa) | 1.93–2.86 | 2.61 | 1.84–2.73 | 1.97 ± 0.05 |
| η (Pa · s) | 2.04–2.99 | 2.36 | 2.01–2.60 | 2.7 ± 0.1 |

elasticity. It can be observed from both of these subplots that the first resonance frequency (f_1) decreases rapidly with an increase in the inclusion radius, as also reported by Hadj Henni *et al* (2010). Such dependence of the first resonance frequency on both inclusion geometry and viscoelasticity parameters is the basis of the ARFIRE inversion process.

Figures 4(d)–(f) display similar plots for HWHM ($B_{1/2}$). These plots of HWHM reveal similar behaviour as the first resonance frequency, i.e. it increases with the storage shear modulus (figure 4(d)), decreases with the inclusion radius modulus (figures 4(e) and (f)), and deviates significantly with variation in viscoelastic properties. Considering these observations, the knowledge of the first resonance frequency alone was not sufficient to simultaneously determine the inclusion elasticity and viscosity, thus justifying the use of the additional parameter $B_{1/2}$, as suggested in this article. The combination of the inclusion radius, elasticity and viscosity provide unique values in the look-up table for the solution of the inverse problem. As seen in figure 4(d), at fixed elasticities and a radius of 5 mm, $B_{1/2}$ increases with the inclusion viscosity, depicting a resonance peak spreading (consistently with a decrease in the quality factor of damped mechanical oscillators).

3.2. Phantom experimental results

This section describes results of the 2.5% gelatin-3% agar inclusion sample experiments. These experiments were conducted to validate the model by testing a sample with known elasticity and viscosity. Figure 5 shows the rheometer data recorded over ~80 min duration, with a processing time step of about 6 min required to reinitialize the instrumentation between each recording (including a 1 min relaxation time). Initially, when the phantom was in a liquid–solid transition state, the measured elasticity was 1.93 kPa. The data was recorded in a controlled environment and the phantom was allowed to gelify naturally. Over time, the elasticity increased exponentially and the last measurement recorded an elasticity of 2.86 kPa. The experiment also suggested that the elasticity increment pattern became almost flat as the gel solidified, as also observed by Genisson *et al* (2006b) and described as a plateau.

The plane wave experiments could be performed only for the gelified phantom (plateau of elasticity). The elasticity and viscosity were measured using the Kelvin–Voigt model in order to be compared with those of Genisson *et al* (2006b). The speed of sound was assumed at 1540 m s^{-1} and the density of the phantom was 1055 kg m^{-3} measured as weight per unit volume. Most similar gelatin-agar phantoms have speed of sound and density in this range (Genisson *et al* 2006b). The velocity and attenuation of shear waves recorded by the ultrasound probe were 1.81 m s^{-1} and 196 Np m^{-1} . The elasticity and viscosity values computed for this experiment are shown in table 2. Rheometry results are also presented in this table for comparison, as long with kinetic measurements performed using the proposed ARFIRE method. It is observed that all three experiments yielded viscoelasticity values in the same range for the gelatin-agar inclusion sample. These values are also comparable to those of Genisson *et al* (2006b) for a similar phantom.

3.3. Blood sample experimental results

Examples of temporal displacements spatially averaged over the inclusion cross-section and acquired over the whole experiment duration, and their corresponding temporal Fourier transforms, are presented in figures 6(a) and (b), respectively. While the delay to obtain the maximum displacement (time-to-peak) remained almost constant after 20 min (figure 6(a)), f_1^{exp} and $B_{1/2}^{\text{exp}}$ varied from 48 Hz to 74 Hz, and from 24 Hz to 45 Hz over that period, respectively (see figure 6(b)). As also observed in panel (b), low frequency components could be seen after 80 min of blood clotting, thus justifying the use of a high-pass filter to determine the first resonance frequency, as mentioned earlier. Furthermore, the choice of $B_{1/2}$ instead of the FWHM clearly appears from these observed low-frequency artifacts. Using the FWHM would have introduced biased values in the inversion process.

Temporal evolutions of f_1^{exp} and $B_{1/2}^{\text{exp}}$, and of estimated blood clot viscoelastic parameters obtained with equation (14), are presented for each experiment of volunteers A and B in figures 7 and 8, respectively. For all experiments, an increase over time of f_1^{exp} and $B_{1/2}^{\text{exp}}$ was observed. This temporal evolution indicates stiffening during coagulation, as depicted by the storage modulus plots. For both volunteers, estimated storage moduli (elasticity) typically varied between 30 Pa and 200 Pa, whereas estimated viscosities were comprised in the range

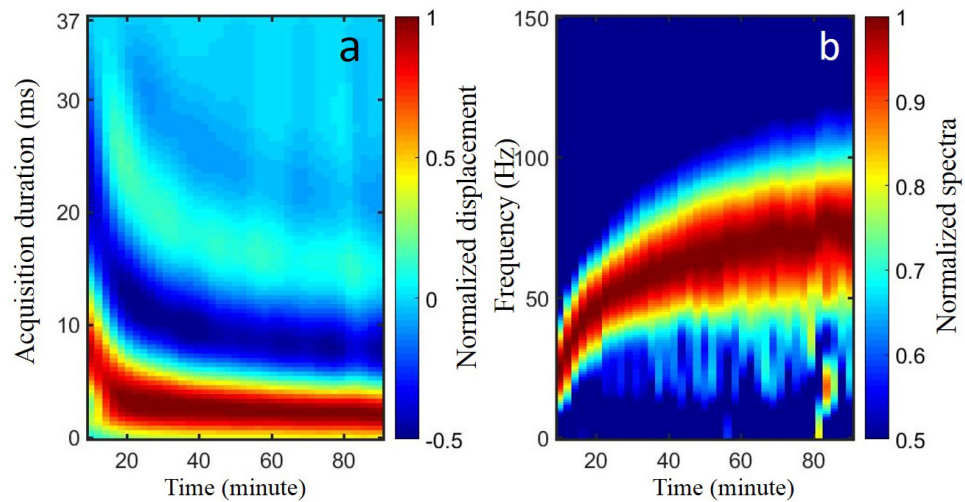


Figure 6. (a) First volunteer, first measurement out of three: experimental normalized temporal displacements $u(t)$ acquired during 37 ms each 2 min during 90 min. (b) Corresponding normalized spectra. Despite a barely constant time-to-peak response observed in the left panel after 20 min, the resonance frequency and spectral width continue to increase (right panel).

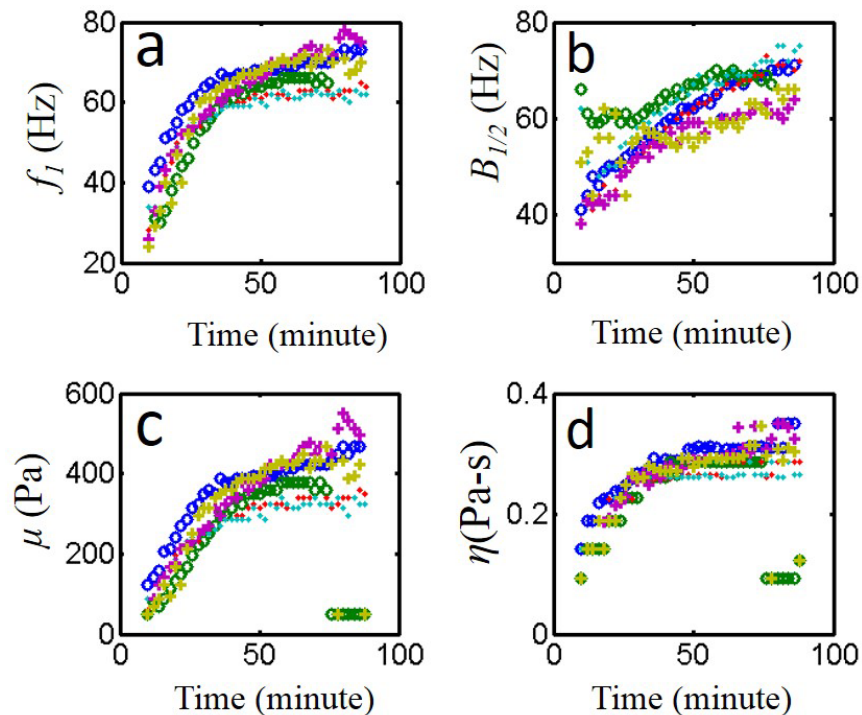


Figure 7. Volunteer A, (a) experimental resonance frequency (f_1) and (b) half width at half maximum ($B_{1/2}$) as a function of clotting time (c) estimated elasticity (μ) and (d) viscosity (η) using the proposed inversion method. Symbols '+', '♦' and 'o' indicate first, second and third experiment over a period of two weeks on each subject's blood. There are two colors per symbol, which indicate two measurements per blood sample withdrawn on a given day.

of 0.1–0.3 Pa · s. The stiffening rates, defined as the slope of $\mu(t)$ in the first 40 min after liquid–gel transition, varied around 8.86 ± 2.04 Pa min⁻¹ for volunteer A, and 5.91 ± 2.21 Pa min⁻¹ for volunteer B. Final viscoelasticity values obtained at the plateau for both volunteers are presented in table 3. For comparison purposes, this table also lists data reported for porcine and rabbit blood in the literature. As seen in both figures 7 and 8, there are a few outliers present in estimated elasticity and viscosity plots. If carefully observed, it could be seen that these outliers correspond to noise/error in the recorded data. For example, for volunteer A (figures 7(a) and (b)), during one measurement (shown with green circles) data was erroneous/incomplete, which causes the outliers in figures 7(c) and (d). The same reason causes the presence of outliers in figure 8 too.

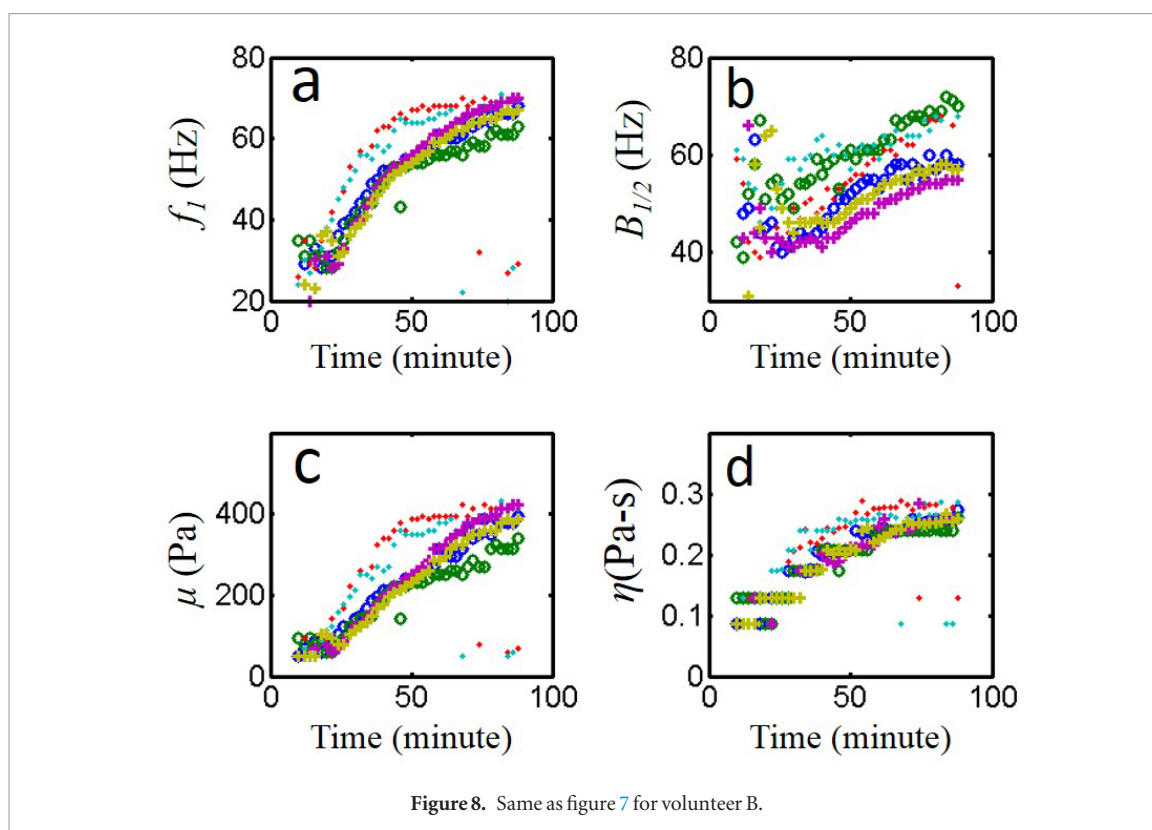


Table 3. Blood clot elasticity and viscosity values obtained with the proposed ARFIRE method and reported in the literature.

| Authors—experiment type | Blood type, HT | Elasticity (Pa) | Viscosity (Pa · s) |
|---|----------------|---------------------|--------------------|
| ARFIRE— <i>in vitro</i> | Human, 38% | 411 ± 71 (A) | 0.25 ± 0.03 (A) |
| | | 387 ± 35 (B) | 0.23 ± 0.02 (B) |
| Huang <i>et al</i> (2013)— <i>in vitro</i> | Porcine, 40% | 196.8 ± 58.4 | 0.29 ± 0.02 |
| Schmitt <i>et al</i> (2007)— <i>in vitro</i> | Porcine, 40% | 943.0 | 0.35 |
| Gennisson <i>et al</i> (2006a)— <i>in vitro</i> | Porcine, 38.4% | 452 ± 15 | 4.3 ± 0.2 |
| Schmitt <i>et al</i> (2013)— <i>ex vivo</i> | Porcine, NA | 498.0 ± 58.0 (IVC) | — |
| | | 436.0 ± 45.0 (RCIV) | — |
| Mfoumou <i>et al</i> (2014)— <i>in vivo</i> | Rabbit, 34% | 1000 ± 600 (JV1) | — |
| | | 25000 ± 6800 (JV2) | — |

HT: Hematocrit.

A: Volunteer A.

B: Volunteer B.

NA: Not available.

IVC: Inferior vena cava.

RCIV: Right common iliac vein.

JV1: Jugular vein after 10 min of clotting.

JV2: Jugular vein after 14 d of clotting.

3.4. Statistical analysis

The coefficient of variation, which expresses dispersion of a random variable relative to its mean value, was computed to effectively assess reproducibility of the results obtained from the human blood measurements. The coefficient of variation was computed as the standard deviation-to-mean ratio of the six measurements of viscoelastic parameters, for each of the two subjects at each time point. A smaller coefficient of variation means that a measured value varies less around its mean value.

The coefficients of variation for elasticity and viscosity measurements of both volunteers' blood samples are shown in figure 9. The temporal plot shows that at each time point after the first 30 min, the dispersion in computed elasticity values around their means was mainly within 10%–20% for volunteer A, and 10%–30% for volunteer B. Similarly, after first 30 min, the variation in viscosity was less than 10% for volunteer A, and less than 20% for volunteer B. Note that blood samples were collected on three different occasions on a two-week period. The plots also indicate that the variation in computed values was higher within the first 30 min, i.e. when blood was in a semi-liquid state. Over the time period when coagulation took effect, precision of the measurements

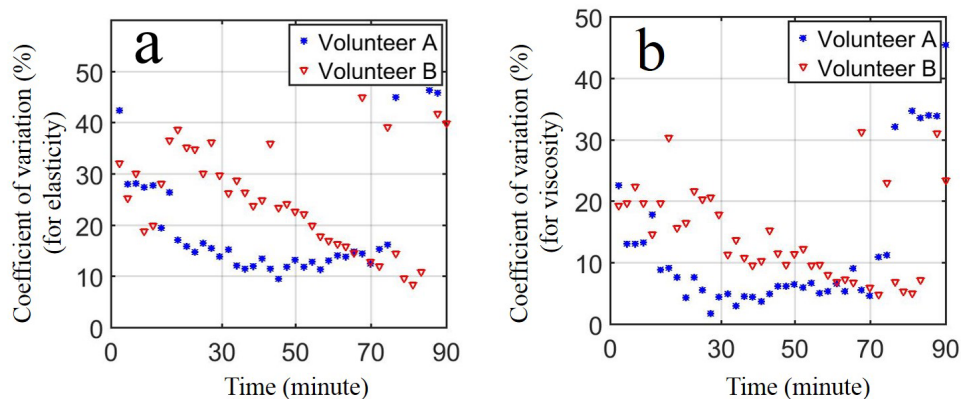


Figure 9. Coefficient of variation plots for subjects A and B of: (a) elasticity; measurements, and (b) viscosity measurements.

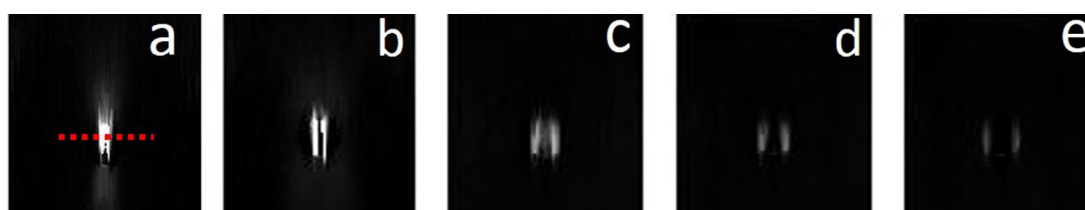


Figure 10. Displacement maps captured at five different points in time. The semi-parallel cylindrical wavefront propagation path can be seen in (a)–(e), which dissipated fast. The inclusion lies along the axis of the red dashed line, as shown in (a).

improved. Since there were a few outliers present in figures 7 and 8 towards the end of the measurement period, this caused presence of high coefficient of variation values for some of the last measurements, as can be seen in figure 9.

4. Discussion

4.1. Observations on experiments with gelatin-agar phantom

The goal of these experiments was to validate the model using an inclusion sample of known viscoelasticity. As seen in figure 5, the rheometry elasticity measurements for the 2.5% gelatin and 3% agar solution displayed an increase in elasticity followed by an asymptotic state, also referred as a plateau. The results obtained from the proposed method were in good agreement with those from the mentioned two reference experiments, and confirmed the validity of the proposed method.

4.2. Observations on experiments with human whole blood

As seen in figures 7 and 8, kinetic measurements recorded from six samples of each volunteer revealed a good reproducibility of viscoelastic parameters over time, which is consistent with the similar hematologic profile of the volunteers (table 1). Typical blood clot kinetic trends were observed, i.e. a fast increase in elasticity and viscosity after the liquid-gel transition followed by an asymptotic behaviour near the plateau region (Ryan *et al* 1999, Gennisson *et al* 2006a, Bernal *et al* 2012). Blood samples from subject B exhibited lower platelet concentration than subject A. Such difference might explain the lower viscoelasticity rates observed in our experiments over the first 40 min after liquid-gel transition, as the platelet count affects blood clot formation (Feghhi and Sniadecki 2011).

A single acoustic radiation force can induce a peak displacement of $5\ \mu\text{m}$ accompanied by a peak temperature increase of $0.04\ ^\circ\text{C}$ – $0.1\ ^\circ\text{C}$ in soft biological tissues (Fahey *et al* 2006, Bouchard *et al* 2009). If the measurement repetition rate and amplitude of the excitation pulse are high, the temperature can increase linearly, and consequently may affect the coagulation process (Palmeri *et al* 2004). Thus, 2 min delay between acquisitions was chosen to lower potential thermal effects on the coagulation process. The magnitude of the displacement caused by a radiation force is inversely proportional to the tissue's mechanical stiffness (Bouchard *et al* 2009). In the beginning of the experiment when blood was in the liquid phase, the radiation pressure push may affect the kinetics by acoustic streaming. However, over time when blood coagulated, the sample became likely less affected by stirring or streaming mechanisms.

In this study, elasticity and viscosity values obtained with human whole blood at 38% hematocrit were in good agreement with values reported for porcine and rabbit blood experiments at the approximately same hematocrit using various techniques (table 3). It is important to note that viscoelasticity values found in the literature strongly depend on the hematocrit. These properties also vary from one subject to another as it can be observed from the different studies listed in table 3. In Gennisson *et al* (2006a), close elasticities were obtained at 38.4% hematocrit, but viscosities of about $4.3 \text{ Pa} \cdot \text{s}$ were documented, which is reasonably greater than results found in the other listed reports. Huang *et al* (2013) found viscosity values in the range of $0.2\text{--}0.4 \text{ Pa} \cdot \text{s}$. The nature of such discrepancy on viscosity was analyzed by Gennisson *et al* (2006a) and attributed to diffraction effects, related to the source directivity. Consequently, measured attenuations produced by viscous effects and diffraction, if not corrected, can lead to an overestimation of the viscosity. This latter issue was recently addressed by our group using a different inverse problem formulation (Kazemirad *et al* 2016). Compared with existing technologies, ARFIRE is based on frequency domain measurements of resonance properties, which is advantageous as the time-domain processing algorithms could be computationally demanding. Also, compared to static or standard dynamic elastography methods, ARFIRE provides the dynamic resonances which can return superior displacement signal-to-noise ratio (Hadj Henni *et al* 2010). During *in vivo* measurements, this could result in optimizing the quality of elastography images, facilitate vascular pathology segmentation, and improve the accuracy in viscoelastic characterization of the tissues. Indeed, a known challenge for elastography methods based on shear wave speed measurements (either through phase shifts or pattern tracking) is the effect of the propagating medium dimension (Chen *et al* 2004). With ARFIRE, a radiation pressure is used to induce mechanical resonance and the spectrum of the displacement map allows determining the first resonance frequency. As discussed earlier, the dimension of the blood clot inclusion may still be a challenge with the proposed method. Indeed, estimated errors increase for small blood clot dimension. The clot dimension can be determined with duplex ultrasound and the vein diameter can be estimated in B-mode and color Doppler can be used to determine residual flow, the remaining lumen structure being the thrombus.

4.3. Perspectives

ARFIRE has been demonstrated to provide a non-invasive method for assessing blood clot viscoelastic properties *ex vivo*, to be applicable to small volumes of blood of about 4 ml without the need to introduce a spherical object inside the sample as in Huang *et al* (2011). It is important to note that the acoustic radiation force generating shear waves is neither a point source nor an infinite length line source. Such source geometry has been modeled in the past, specifically in geophysical applications (Hazebroek 1966, Viswanathan 1970, and Abozena 1977). In the analytical model developed in this study, the source was considered as a line source, which generates cylindrical wavefronts. The depth of the acoustic radiation force was between 3–5 mm, while the diameter of the inclusion was 5 mm. Thus, a cylindrical wavefront approximation was considered since the inclusion diameter and the depth of the radiation force were of the same order of magnitude. A displacement map of shear waves propagating in a human blood sample experiment is shown in figure 10, which supports the assumption of cylindrical wavefronts. The experimental results were also in good agreement with the theoretical prediction, which further demonstrates the soundness of the proposed analytical model. Moreover, the accuracy of the model was confirmed by results obtained from the gelatin-agar phantom experiments. A 1D simplification of the presented model is provided in appendix C, which aims at exploring the proposed analytical scattering model in a simplified way.

The current model would also be valid if a pushing sequence similar to that generated in supersonic shear imaging (SSI) is used to induce shear waves instead of a single acoustic push. In fact, in the case of an inclusion with a larger diameter, it would be better to use an SSI sequence, as a larger acoustic radiation force depth is induced. The cylindrical wavefront assumption would be even more justified in that case, as was also assumed in prior literature (Kazemirad *et al* 2016, Bernard *et al* 2017).

Considering cylindrical geometries with the ARFIRE analytical model implicitly assumes blood clots to be totally occlusive. However, the presence of residual flow and an irregular geometry of the thrombus in contact with blood may still be considered but errors in viscoelasticity estimates would occur. Partial occluding thrombi were addressed in the past with an inverse problem formulation considering finite-element modeling (Schmitt *et al* 2013). Such configurations might be challenging for an analytical approach due to variable boundary conditions (fluid or elastic) over the inclusion contour. Elliptical blood clot geometries were described in duplex ultrasound imaging (Comerota *et al* 1993). In such cases, it may be possible to adapt ARFIRE to consider ellipsoids. Shear wave scattering by elliptical structures was previously investigated in the case of plane incident shear waves (Montagnon *et al* 2013). This may constitute a framework to adapt ARFIRE for future works.

The estimation of stage and maturity of DVT is critical in determining the therapeutic management. DVT in acute phase carries greater risk of pulmonary embolism and requires immediate anticoagulation treatment with heparin. Staging of DVT still remains mostly qualitative and non-standardized, and measuring this quantity is clinically extremely desirable (Hoang *et al* 2017). The viscoelastic properties of thrombus change with its age, and

this could be a surrogate marker for the chronicity of a clot. A broader study with more human subjects demonstrated a statistically significant difference between acute and chronic clots, as suggested by the results of Yi *et al* (2017). This latter group studied 127 subjects with DVT and used strain elastography to measure differences in thrombus age. The clinical translation of any DVT diagnosis technique would require addressing this challenge. It is noteworthy that in the proposed ARFIRE technique, the resonance frequency depends on the inclusion diameter and stiffness, which can provide information on size and stage of the thrombus. The resonance frequencies occurring in the lower spectrum suggest an early blood clot in acute phase, while a higher resonance frequency suggests a matured and stiffer clot. However, resonance may occur at very high frequencies in very stiff thrombi, which may make measurements difficult. The other silver lining is that ARFIRE can measure the size of the blood clot. However, the heterogeneous nature of the different pathological constituents in the tissue and its non-uniform shape can still be a challenge for *in vivo* measurements. Thus, further studies with larger population of human subjects are necessary to assess the accuracy and reproducibility of the proposed technique. Overall, this technique carries the potential for this translation, as suggest the results of the present study.

5. Conclusion

A theoretical framework and *ex vivo* results on the viscoelastic characterization of coagulating blood based on a mechanical resonance induced by an acoustic radiation force excitation have been presented in this article. The main aim of this study was to assess the capability of such resonance elastography method, which can provide an alternative to conventional rheology techniques. The proposed ARFIRE method reported rheology measures on gelatin-agar gels and blood clots in a range of frequency between 50–150 Hz, typically. The proposed method also allowed monitoring the temporal kinetics of both elasticity and viscosity of human clotting whole blood. It is envisaged that this method may allow staging acute thrombus property, monitoring response to medication or assessing embolization risk. More generally, the proposed method has the potential to characterize viscoelastic properties of a variety of soft biological tissues.

Acknowledgments

This work was supported by the Canadian Institutes of Health Research (grant #MOP-84358).

Appendix A. Application of Graf's addition theorem

The Graf's addition theorem (Abramowitz and Stegun 1980) for Hankel functions is expressed in equation (2), which describes the addition rule. The corresponding diagram is shown in figure A1(a). This equation can be utilized to derive an expression for the current framework to write equation (2) in the coordinate system of the inclusion (thrombus) (r_k, θ_k, z_k) .

Figure A1(b) explains the geometry of the current problem. The z -axis of the cylindrical inclusion is in the z_k direction. The other two coordinate axes of this system are denoted as r_k, θ_k in the figure. The cylindrical coordinate system along the acoustic radiation force has its longitudinal axis (z_j) perpendicular to the z_k -axis of the inclusion's coordinate system. The radius of this system is denoted as r_j in the figure. Clearly, triangle OCB forms a right angle triangle. Thus, using the addition theorem, the Hankel function given in equation (2) can be transformed to the (r_k, θ_k, z_k) coordinate system. Thus, for the plane $OCBO$, using equation (3) for $n = 0$ and within the condition $|z_k| < |r_k \sin \theta_k|$

$$H_0(k_s r_j) = \sum_{m=-\infty}^{\infty} J_m(k_s z_k) H_m(k_s r_k \sin \theta_k) e^{im\pi/2}, \quad (\text{A.1})$$

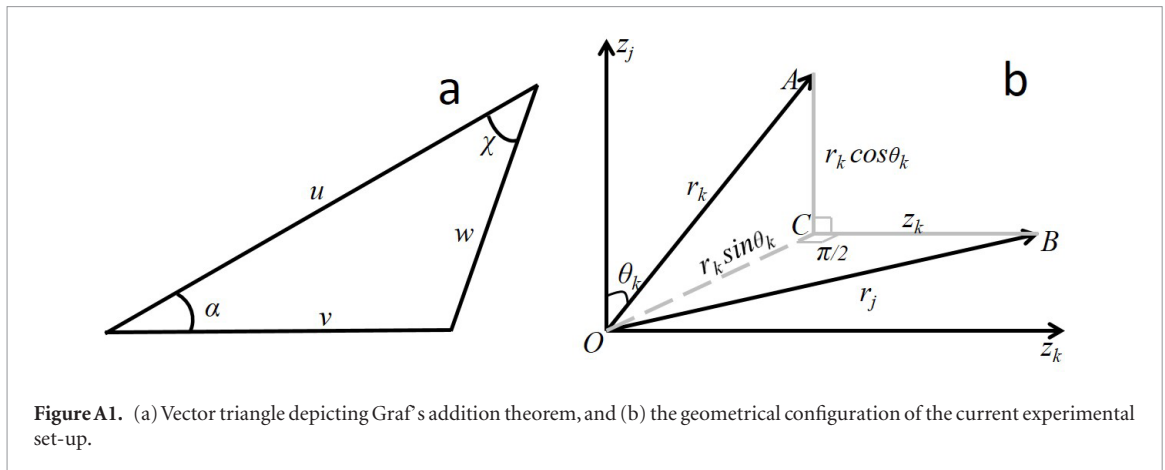
where, $\pi/2$ is the angle between the connecting vector $r_k \sin \theta_k$ and z_k in the plane $OCBO$.

Now, the expression of equation (A.1) can be used in equation (2) to update the incident wave equation. This results in the following equation, which is given as equation (3) in the main text:

$$U_{\text{inc}}(r, \omega) = A_1(\omega) \frac{i}{4} \sum_{m=-\infty}^{\infty} J_m(k_s z_k) H_m^{(1)}(k_s r_k \sin \theta_k) e^{\frac{im\pi}{2}}.$$

Appendix B. Computation of the stress tensor

The strain gradient theory in the cylindrical coordinate system has been described in detail by Zhao and Pedroso (2008), which explains the computation of the gradient of the displacement vector and the stiffness tensor \mathbf{C} . This appendix briefly lists the formulae that are required in the current framework.



The right-hand side of equation (12) layouts the tensor components of \mathbf{C} and ϵ . For the stiffness tensor matrix \mathbf{C} ,

$$\begin{aligned} C_{rr} &= \lambda + 2G \\ C_{r\theta} &= C_{\theta r} = \lambda ; \\ \frac{C_{rr} - C_{r\theta}}{2} &= G \end{aligned} \quad (\text{B.1})$$

where, λ , G are first and second Lamé coefficients. The elements of the strain tensor ϵ , which involve the partial derivatives of the displacement vector (equations (3)–(5)), are given as Zhao and Pedroso (2008)

$$\begin{aligned} \epsilon_{rr} &= \frac{\partial u_r}{\partial r}; \quad \epsilon_{\theta\theta} = \frac{1}{r} \frac{\partial u_\theta}{\partial r} + \frac{u_r}{r}; \quad \epsilon_{zz} = \frac{\partial u_z}{\partial z}; \quad \epsilon_{r\theta} = \epsilon_{\theta r} = \frac{1}{2} \left(\frac{1}{r} \frac{\partial u_r}{\partial \theta} + \frac{\partial u_\theta}{\partial r} - \frac{u_\theta}{r} \right); \\ \epsilon_{rz} &= \epsilon_{zr} = \frac{1}{2} \left(\frac{\partial u_r}{\partial z} + \frac{\partial u_z}{\partial r} \right); \text{ and } \epsilon_{\theta z} = \epsilon_{z\theta} = \frac{1}{2} \left(\frac{\partial u_\theta}{\partial z} + \frac{1}{r} \frac{\partial u_z}{\partial \theta} \right). \end{aligned} \quad (\text{B.2})$$

Here, u_r, u_θ, u_z are directional components of the displacement vector. Note that displacement components u_r and u_θ are zero in the case of a cylindrical shear wave propagation, as the particle displacement is only in the z -direction (u_z), which is expressed in equations (3)–(5). Thus, to implement the boundary condition of equation (11), the stress tensor $\sigma = \mathbf{C}\epsilon$ can be calculated using above mentioned formulae. As a general form, this equation can also be written as

$$\sigma = \mathbf{C}\epsilon = \mathbf{C} \frac{1}{2} \{ (\nabla U)^T + \nabla U \}. \quad (\text{B.3})$$

As seen in equations (3)–(5), displacement vectors contain scattering and transmission coefficients. Hence, similar to how equation (10) is achieved, when equation (B.3) is substituted into equation (11) for incident, reflected, and transmitted wave equations, it yields a linear equation with two unknowns $A(\omega)$ and $B(\omega)$, as for the second boundary condition. For example, considering the stress component σ_{rz} , this stress continuity boundary condition can be written in the form

$$G_{\text{inc}} \frac{\partial u_{\text{inc}}}{\partial r} + G_{\text{inc}} \frac{\partial u_{\text{ref}}}{\partial r} = G_{\text{surr}} \frac{\partial u_{\text{trans}}}{\partial r},$$

where G_{inc} and G_{surr} are second Lamé coefficients coming from equation (B.1) for the inclusion and surrounding medium, respectively.

Appendix C. 1D simplification of the analytical model

The proposed analytical model allowed determining first resonance frequencies for various inclusion dimensions and viscoelastic properties. The elasticity and radius were shown to be the main parameters affecting the first resonance frequency (figure 4). For fixed values of these parameters, the viscosity had slight impact on f_1 for tested experimental conditions (figure 4(a)). The following discussion aims to determine if an oversimplification of the 2D analytical scattering model could provide another way to study the problem in hand. The resonance frequency $f_1(r, \mu)$ presented in figure 4 can indeed be simplified in 1D by assuming an equivalent vibrating string instead of the 2D cylindrical geometry considered in this work. The simplified 1D equation is expressed as

$$f_1 = \alpha \sqrt{\frac{\mu}{\rho}} + \beta, \quad (\text{C.1})$$

with α and β being two constants to be determined. Fitting resonance frequencies in the ranges $r \in [3, 8]$ mm (0.5 mm stepwise) and $\mu \in [50, 500]$ Pa (25 Pa stepwise) using equation (C.1) gives $\alpha = 1.72$ and $\beta = 0.30$. Such constants lead to $0.40 \pm 0.31\%$ mean errors on estimated f_1 over the whole investigated grid of (r, μ) , when

comparing the 2D problem to its 1D simplification. Equation (C.1) thus appears as a reliable fitting function in studied ranges to estimate the storage shear modulus; this latter equation can indeed be rewritten as

$$\mu(f_1, r) = 4\rho r^2 \frac{(f_1 - \beta)^2}{\alpha^2}. \quad (\text{C.2})$$

By assuming that the inclusion density ρ is known, and because $\beta \ll f_1$, one can write

$$d\mu(f_1, r) = \frac{\partial\mu}{\partial f_1} df_1 + \frac{\partial\mu}{\partial r} dr, \quad (\text{C.3})$$

$$\frac{d\mu}{\mu} = 2 \left(\frac{df_1}{f_1} + \frac{dr}{r} \right). \quad (\text{C.4})$$

From equation (C.4), it appears that the error on estimating the elasticity (storage shear modulus) is tightly bounded to errors on both resonance frequency and inclusion radius measurements. Such behaviour suggests a low accuracy on the elasticity estimation for very small radii. As depicted in figure 4, the 1D simplification to retrieve an expression for $B_{1/2}$ is much more complex as this parameter has complicated and strong dependence on the inclusion elasticity, viscosity and radius. Estimating bounding error values with a 1D model simplification is not attempted here; the general behaviour of $B_{1/2}$ can be seen on figures 4(d)–(f).

At this point, the effect of surrounding medium mechanical properties on both f_1 and $B_{1/2}$ has not yet been investigated. To answer this issue, both parameters were estimated considering an inclusion radius of 5 mm, an elasticity of 200 Pa, and a viscosity of 0.15 Pa · s, embedded in an infinite surrounding medium with an elasticity varying between 3000 and 10 000 Pa, and a viscosity ranging from 0.01 to 1 Pa · s. Analytically computed first resonance frequencies varied by only 2% or less, which strongly indicate that changing surrounding medium mechanical parameters only affects the ratio of transmitted and reflected waves at boundaries but not the shear wave speed inside the inclusion. These observations are in agreement with previous results (Schmitt *et al* 2013). On the other hand, over tested surrounding medium elasticity and viscosity values, $B_{1/2}$ increased from 20 Hz to 31 Hz with changes in elasticity, and remained relatively constant with varying viscosity (changes below 2%). Such dependencies make us conclude that blood clot viscoelasticity can accurately be assessed even if some uncertainties exist on the viscoelasticity of surrounding muscles and biological tissues of the lower limbs.

ORCID iDs

Guy Cloutier  <https://orcid.org/0000-0002-4957-4844>

References

- Abozena A M 1977 Radiation from a finite cylindrical explosive source *Geophysics* **42** 1384–93
- Abramowitz M and Stegun I A 1980 *Handbook of Mathematical Functions with Formulas, Graphs, and Mathematical Tables* (New York: Dover) p 363
- Aglyamov S R, Karpouk A B, Ilinskii Y A, Zabolotskaya E A and Emelianov S Y 2007 Motion of a solid sphere in a viscoelastic medium in response to applied acoustic radiation force: theoretical analysis and experimental verification *J. Acoust. Soc. Am.* **122** 1927–36
- Aki K and Richards P G 1980 *Quantitative Seismology: Theory and Methods* (San Francisco, CA: Freeman) p 196
- Anand M and Rajagopal K R 2017 A short review of advances in the modelling of blood rheology and clot formation *Fluids* **2** 35
- Andreev V G, Dmitriev V N, Pischalnikov Y A, Rudenko O V, Sapozhnikov O A and Sarvazyan A P 1997 Observation of shear waves excited by focused ultrasound in rubber-like medium *Acoustic. Phys.* **43** 123–8
- Benes J, Zatloukal J and Kletecka J 2015 Viscoelastic methods of blood clotting assessment—a multidisciplinary review *Frontiers Med.* **2** 62
- Bernal M, Gennisson J L, Flaud P and Tanter M 2012 Shear wave elastography quantification of blood elasticity during clotting *Ultrasound Med. Biol.* **38** 2218–28
- Bernal M, Gennisson J L, Flaud P and Tanter M 2013 Correlation between classical rheometry and supersonic shear wave imaging in blood clots *Ultrasound Med. Biol.* **39** 2123–36
- Bernard S, Kazemirad S and Cloutier G 2017 A frequency shift method to measure shear-wave attenuation in soft tissues *IEEE Trans. Ultrason. Ferroelectr. Freq. Control* **64** 514–24
- Bouchard R R, Dahl J J, Hsu S J, Palmeri M L and Trahey G E 2009 Image quality, tissue heating, and frame rate trade-offs in acoustic radiation force impulse imaging *IEEE Trans. Ultrason. Ferroelectr. Freq. Control* **56** 63–76
- Catheline S, Gennisson J L, Delon G, Fink M, Sinkus R, Abouelkaram S and Culioli J 2004 Measurement of viscoelastic properties of homogeneous soft solid using transient elastography: an inverse problem approach *J. Acoust. Soc. Am.* **116** 3734–41
- Chen S, Fatemi M and Greenleaf J F 2004 Quantifying elasticity and viscosity from measurement of shear wave speed dispersion *J. Acoust. Soc. Am.* **115** 2781–5
- Comerota A J, Katz M L and Hashemi H A 1993 Venous duplex imaging for the diagnosis of acute deep venous thrombosis *Pathophysiol. Haemost. Thromb.* **23** 61–71
- Emelianov S Y, Chen X, O'Donnell M, Knipp B, Myers D, Wakefield T W and Rubin J M 2002 Triplex ultrasound: elasticity imaging to age deep venous thrombosis *Ultrasound Med. Biol.* **28** 757–67
- Erdelyi A 1968 *Higher Transcendental Functions* vol II (New York: McGraw-Hill) pp 44–5
- Esmon C T 2009 Basic mechanisms and pathogenesis of venous thrombosis *Blood Rev.* **23** 225–9

- Fahey B J, Palmeri M L and Trahey G E 2006 Frame rate considerations for real-time abdominal acoustic radiation force impulse imaging *Ultrason. Imaging* **28** 193–210
- Feghhi S and Sniadecki N J 2011 Mechanobiology of platelets: techniques to study the role of fluid flow and platelet retraction forces at the micro- and nano-scale *Int. J. Mol. Sci.* **12** 9009–30
- Galanau J P, Laroche J P and Righini M 2013 The history and historical treatments of deep vein thrombosis *J. Thromb. Haemost.* **11** 402–11
- Gennisson J L and Cloutier G 2006b Sol-gel transition in agar-gelatin mixtures studied with transient elastography *IEEE Trans. Ultrason. Ferroelectr. Freq. Control* **53** 716–23
- Gennisson J L, Lerouge S and Cloutier G 2006a Assessment by transient elastography of the viscoelastic properties of blood during clotting *Ultrasound Med. Biol.* **32** 1529–37
- Gennisson J L, Marcellan A, Dizeux A and Tanter M 2014 Rheology over five orders of magnitude in model hydrogels: agreement between strain-controlled rheometry, transient elastography, and supersonic shear wave imaging *IEEE Trans. Ultrason. Ferroelectr. Freq. Control* **61** 946–54
- Goldenberg N A and Manco-Johnson M J 2008 Protein C deficiency *Haemophilia* **14** 1214–21
- Graff K F 1991 *Wave Motion in Elastic Solids* (New York: Dover) pp 283–6
- Hadj Henni A, Schmitt C and Cloutier G 2010 Shear wave induced resonance elastography of soft heterogeneous media *J. Biomech.* **43** 1488–93
- Hadj Henni A, Schmitt C, Tremblay M E, Hamdine M, Heuzey M C, Carreau P and Cloutier G 2011 Hyper-frequency viscoelastic spectroscopy of biomaterials *J. Mech. Behav. Biomed. Mater.* **4** 1115–22
- Hadj Henni A, Schmitt C, Trop I and Cloutier G 2012 Shear wave induced resonance elastography of spherical masses with polarized torsional waves *Appl. Phys. Lett.* **100** 133702
- Hajjarian Z, Tripathi M M and Nadkarni S K 2015 Optical thromboelastography to evaluate whole blood coagulation *J. Biophotonics* **8** 372–81
- Hazebroek P 1966 Elastic waves from a finite line source *Proc. R. Soc. A* **294** 38–65
- Heijboer H, Brandjes D P M, Büller H R, Sturk A and ten Cate J W 1990 Deficiencies of coagulation-inhibiting and fibrinolytic proteins in outpatients with deep-vein thrombosis *N. Engl. J. Med.* **323** 1512–6
- Heit J, Silverstein M D, Mohr D N, Petterson T M, O'Fallon W and Melton L 2000 Risk factors for deep vein thrombosis and pulmonary embolism: a population-based case-control study *Arch. Intern. Med.* **160** 809–15
- Hirsh J and Hoak J 1996 Management of deep vein thrombosis and pulmonary embolism: a statement for healthcare professionals from the council on thrombosis (in consultation with the council on cardiovascular radiology) *Circulation* **93** 2212–45
- Hoang P, Wallace A, Sugi M, Fleck A, Pershad Y, Dahiya N, Albadawi H, Knuttinen G, Naidu S and Oklu R 2017 Elastography techniques in the evaluation of deep vein thrombosis *Cardiovasc. Diagn. Ther.* **7** S238–45
- Huang C C, Chen P Y and Shih C C 2013 Estimating the viscoelastic modulus of a thrombus using an ultrasonic shear-wave approach *Med. Phys.* **40** 42901–7
- Huang C C, Shih C C, Liu T Y and Lee P Y 2011 Assessing the viscoelastic properties of thrombus using a solid-sphere-based instantaneous force approach *Ultrasound Med. Biol.* **37** 1722–33
- Jentschura U D and Lotstedt E 2011 Numerical calculation of Bessel, Hankel and Airy functions *Comput. Phys. Commun.* **183** 506–19
- Karande G Y, Hedgire S S, Sanchez Y, Baliyan V, Mishra V, Ganguli S and Prabhakar A M 2016 Advanced imaging in acute and chronic deep vein thrombosis *Cardiovasc. Diagn. Ther.* **6** 493–507
- Kazemirad S, Bernard S, Hybois S, Tang A and Cloutier G 2016 Ultrasound shear wave viscoelastography: model-independent quantification of the complex shear modulus *IEEE Trans. Ultrason. Ferroelectr. Freq. Control* **63** 1399–408
- Luo J and Konofagou E E 2010 A fast normalized cross-correlation calculation method for motion estimation *IEEE Trans. Ultrason. Ferroelectr. Freq. Control* **57** 1347–57
- Mfomou E, Tripette J, Blostein M and Cloutier G 2014 Time-dependent hardening of blood clots quantitatively measured *in vivo* with shear wave ultrasound imaging in a rabbit model of venous thrombosis *Thromb. Res.* **133** 265–71
- Montagnon E, Hadj H A, Schmitt C and Cloutier G 2013 Viscoelastic characterization of elliptical mechanical heterogeneities using a semi-analytical shear-wave scattering model for elastometry measures *Phys. Med. Biol.* **58** 2325–48
- Montagnon E, Hissoiny S, Despres P and Cloutier G 2012 Real-time processing in dynamic ultrasound elastography: a GPU-based implementation using CUDA *11th Int. Conf. Information Science, Signal Processing and their Applications (ISSPA) (Montreal, QC)* pp 472–7
- Morse P M and Feshbach H 1953 *Methods of Theoretical Physics* (New York: McGraw-Hill) ch 11.2
- Mumme A, Heinen W, Geier B, Maatz W, Barbera L and Walterbusch G 2002 Regional hyperthermic fibrinolytic perfusion after unsuccessful venous thrombectomy of extensive deep venous thrombosis *J. Vasc. Surg.* **36** 1219–24
- Naess I A, Christiansen S C, Romundstad P, Cannegieter S C, Rosendaal F R and Hammerstrom J 2007 Incidence and mortality of venous thrombosis: a population-based study *J. Thromb. Haemost.* **5** 692–9
- Orescanin M, Toohey K S and Insana M F 2009 Material properties from acoustic radiation force step response *J. Acoust. Soc. Am.* **125** 2928–36
- Palmeri M L and Nightingale K R 2004 On the thermal effects associated with radiation force imaging of soft tissue *IEEE Trans. Ultrason. Ferroelectr. Freq. Control* **51** 551–65
- Ribreau C and Thiriet M 1998 *Écoulements Veineux. In Biomécanique des Fluides et des Tissus* ed M Y Faffrin and F Goubel (Paris: Masson)
- Rubin J M, Xie H, Kim K, Weitzel W F, Emelianov S Y, Aglyamov S R, Wakefield T W, Urquhart A G and O'Donnell M 2006 Sonographic elasticity imaging of acute and chronic deep venous thrombosis in humans *J. Ultrasound Med.* **25** 1179–86
- Ryan E A, Mockros L F, Weisel J W and Lorand L 1999 Structural origins of fibrin clot rheology *Biophys. J.* **77** 2813–26
- Schmitt C, Hadj H A and Cloutier G 2007 Characterization of time-varying mechanical viscoelastic parameters of mimicking deep vein thrombi with 2D dynamic elastography *IEEE Ultrasonics Symp. Proc. (New York, NY)* pp 1009–12
- Schmitt C, Hadj H A and Cloutier G 2011 Characterization of blood clot viscoelasticity by dynamic ultrasound elastography and modeling of the rheological behavior *J. Biomech.* **44** 622–9
- Schmitt C, Montagnon E, Hadj H A, Qi S and Cloutier G 2013 Shear wave induced resonance elastography of venous thrombi: a proof-of-concept *IEEE Trans. Med. Imaging* **32** 565–77
- Siebers S, Geier B, Scheipers U, Vogt M, Mumme A and Ermert H 2004 Classification of venous thrombosis combining ultrasound elastography and tissue characterization *IEEE Ultrasonics Symp. 2004* vol 3 pp 1761–4
- Valeri C R, MacGregor H, Cassidy G, Tinney R and Pompei F 1995 Effects of temperature on bleeding time and clotting time in normal male and female volunteers *Crit. Care Med.* **23** 698–704
- Viola F and Walker W F 2003 A comparison of the performance of time-delay estimators in medical ultrasound *IEEE Trans. Ultrason. Ferroelectr. Freq. Control* **50** 392–401

- Viola F, Kramer M D, Lawrence M B, Oberhauser J P and Walker W F 2004 Sonorheometry: a noncontact method for the dynamic assessment of thrombosis *Ann. Biomed. Eng.* **32** 696–705
- Viswanathan K 1970 On elastic waves from a finite line-source *Proc. Camb. Phil. Soc.* **67** 209–14
- Voronovich A G 1999 *Wave Scattering from Rough Surfaces* (Berlin: Springer)
- Weisel J W 2008 Enigmas of blood clot elasticity *Science* **320** 456–7
- White R H 2003 The epidemiology of venous thromboembolism *Circulation* **107** 14–8
- Xie H *et al* 2004 Staging deep venous thrombosis using ultrasound elasticity imaging: animal model *Ultrasound Med. Biol.* **30** 1385–96
- Xie H, Kim K, Aglyamov S R, Emelianov S Y, O'Donnell M, Weitzel W F, Wroblewski S K, Myers D D, Wakefield T W and Rubin J M 2005 Correspondence of ultrasound elasticity imaging to direct mechanical measurement in aging DVT in rats *Ultrasound Med. Biol.* **31** 1351–9
- Xu X, Zhu J and Chen Z 2016 Dynamic and quantitative assessment of blood coagulation using optical coherence elastography *Sci. Rep.* **6** 24294
- Yamada Y and Hidaka T 2005 Reflection of a spherical wave by acoustically hard, concave cylindrical walls based on the tangential plane approximation *J. Acoust. Soc. Am.* **118** 818–31
- Yi X, Wei X, Wang Y, Chen J, Li D and Hu B 2017 Role of real-time elastography in assessing the stage of thrombus *Int. Angiol.* **36** 59–63
- Zhao J and Pedrosa D 2008 Strain gradient theory in orthogonal curvilinear coordinates *Int. J. Solid Struct.* **45** 3507–20